bioRxiv preprint doi: https://doi.org/10.1101/2021.05.09.442953; this version posted May 9, 2021. The copyright holder for this preprint (which was not certified by peer review) is the author/funder, who has granted bioRxiv a license to display the preprint in perpetuity. It is made available under aCC-BY-NC-ND 4.0 International license.

# Stress-induced protein disaggregation in the Endoplasmic Reticulum catalysed by BiP

**Eduardo Pinho Melo[1, 2*], Ilaria Farace[1], Tasuku Konno[1], Mosab Ali Awadelkareem[1], Lise R. Skov[1], Teresa P. Sancho[2], Adrienne W. Paton[3], James C. Paton[3], Matthew Fares[4], Pedro M. R. Paulo[5], Xin Zang[4] & Edward Avezov[1 *]**

[1] UK Dementia Research Institute at University of Cambridge, Department of Clinical Neurosciences, Cambridge CB2 0AH, United Kingdom

[2] CCMAR-Centro de Ciências do Mar, Universidade do Algarve, Campus de Gambelas, 8005-139 Faro, Portugal

[3] Research Centre for Infectious Diseases, Department of Molecular and Biomedical Science, University of Adelaide, Adelaide, SA, 5005, Australia

[4] Department of Chemistry, The Pennsylvania State University, University Park, Pennsylvania

[5] Centro de Química Estrutural, Instituto Superior Técnico, Universidade de Lisboa, Av. Rovisco Pais, 1049-001 Lisboa, Portugal

[*]Address correspondence to: Edward Avezov and Eduardo Pinho Melo

bioRxiv preprint doi: https://doi.org/10.1101/2021.05.09.442953; this version posted May 9, 2021. The copyright holder for this preprint (which was not certified by peer review) is the author/funder, who has granted bioRxiv a license to display the preprint in perpetuity. It is made available under aCC-BY-NC-ND 4.0 International license.

## Abstract:

Protein synthesis is supported by cellular machineries that ensure polypeptides fold to their native three-dimensional conformation with high fidelity whilst eliminating misfolded, aggregation-prone species. While protein aggregates can contribute to pathologies exemplified by Alzheimer's and Parkinson's diseases, their abundance is normally minimised by molecular chaperones such as HSP70/90, which promote native folding and drive the recycling of aberrantly folded species. Cytoplasmic chaperones (e.g. HSP70/40) can resolve insoluble protein aggregates should the preventive mechanisms falter. However, it is unknown whether an analogous disaggregation system is needed and exists in the Endoplasmic Reticulum (ER), where ~30% of the proteome is synthesised. Here we show that the ER of a variety of mammalian cell types, including neurons, is endowed with the capability to resolve protein aggregates that accumulate upon expression of metastable proteins. Utilising a purpose-developed protein aggregation probing system with a sub-organellar resolution, we observed steady-state aggregate accumulation in the ER. Strikingly, pharmacological induction of ER stress did not augment aggregates but rather stimulated their clearance within hours. We found that this disaggregation activity was catalysed by the stress-responsive ER molecular chaperone – BiP. Its elimination abolished the disaggregation activity in cells. Further, we reconstructed the disaggregation-reaction *in-vitro* by a minimal system of ATP-fuelled BiP and its J-protein cofactor. These data reveal a hitherto unknown, non-redundant function of the ER stress response. Thus, our findings may facilitate the identification of aggregation-antagonising strategies and rationalising the age-dependent protein misfolding pathology.

**Summary:** ER stress induction activates a protein disaggregation machinery, powered by BiP – an abundant ER chaperone, revealed by a FLIM-based protein aggregation monitoring in live cells.

bioRxiv preprint doi: https://doi.org/10.1101/2021.05.09.442953; this version posted May 9, 2021. The copyright holder for this preprint (which was not certified by peer review) is the author/funder, who has granted bioRxiv a license to display the preprint in perpetuity. It is made available under aCC-BY-NC-ND 4.0 International license.

## Results and discussion:

Newly synthesised polypeptides must attain the functional three-dimensional conformation, thermodynamically encoded by the amino acid sequence[1]. The accepted model of protein folding describes the process where polypeptides seek the minimum point in energy-funnel but can be trapped in local minima separated by low barriers (misfolding traps[2]). Furtherer, the chemical diversity and crowdedness of cellular compartments create conditions for reactions competing with native folding, inducing local unfolding and stabilising non-functional, misfolding-trapped conformations. Unfolded and misfolded protein species tend to form insoluble aggregates[3]. To avoid the accumulation of cytotoxic aggregates, the biosynthetic organelles (i.e., cytoplasm, the Endoplasmic Reticulum, ER, and mitochondria) evolved a multi-layer proteostasis network (PN) that chaperones nascent proteins and rescues or recycles misfolded intermediates[4]. The PN is endowed with a capability to feedback to the gene-transcription and translation systems to interactively adjust the protein production rate to its folding-assistance and quality control capability. The ER branch of the PN, the Unfolded Protein Response (UPR), alleviates un/misfolded protein load during stress by transient attenuation of protein synthesis and posttranslational chaperone activation, followed by transcriptional upregulation of protein maturation and quality control factors[5,6].

Shortfalls of the PN machinery may lead to pathology: protein aggregation accompanies neurodegenerative diseases such as Alzheimer's, Parkinson's, Amyotrophic Lateral Sclerosis and Frontotemporal Dementia[7]. Neuronally expressed metastable proteins (e.g. Aβ, Tau, or α-synuclein) – with a tendency to oligomerise and consequently aggregate – underlie these conditions. The late onset of the aggregation-related sub-populational neurodegeneration is consistent with age- and environmental factor-dependent decline in the efficiency of the PN machinery. Understanding how the cell handles aggregation-prone proteins on an organellar level is crucial to rationalising the disease-related proteostasis impairment.

The recent discovery of the cytosolic Hsp70 chaperone and its assisting system's capacity to resolve cytoplasmic aggregates[8] (including amyloids[9,10]) adds another functional layer to the PN for rectifying imperfections of the quality control system or prion-like transition from native folding to aggregation. However, it is unknown whether such a capability exists in the ER – a site responsible for the manufacturing of about one-third of the cell's protein repertoire (including disease determinants, e.g., amyloid precursor protein, APP). Observations suggest that the chaperone-reach environment of the ER is more immune to protein aggregation than the cytoplasm[11]. How the organelle maintains high fidelity protein folding, avoiding aggregation throughout the lifetime of the cell, particularly the non-dividing neurons, remains an open question. Explaining this in terms of protein folding quality control alone would rest on the assumption that the system can achieve zero aggregation and absolute quality control through astronomically large numbers of protein folding cycles.

To address how the ER handles protein folding/aggregation, we established an optical approach to monitoring this process in live cells based on a cell-inert metastable surrogate protein. The protein core of the probe is an *E. coli* haloalkane dehydrogenase

bioRxiv preprint doi: https://doi.org/10.1101/2021.05.09.442953; this version posted May 9, 2021. The copyright holder for this preprint (which was not certified by peer review) is the author/funder, who has granted bioRxiv a license to display the preprint in perpetuity. It is made available under aCC-BY-NC-ND 4.0 International license.

variant destabilised by mutagenesis and covalently modifiable by a solvatochromic fluorescent moiety (Fig. 1a,[12]) HT-aggr herein. As HT-aggr has no natural function and interactors in the ER, its fate (in terms of folding, aggregation, and degradation) is exclusively reflective of the protein-handling activity in the host organelle.

The aggregation propensity of the HT-aggr probe is predicted by a relatively low unfolding free energy value ($\Delta G^0_{unf}$ decreased from 5.6 kcal/mol in WT-HT to 2.0 kcal/mol in HT-aggr K73T, Fig. S1). This metastability – propensity to aggregate, was reflected in fluorescence correlation spectroscopy (FCS) measurements: upon heating *in-vitro*, HT-aggr formed particles with a hydrodynamic radius (Rh) of 48 nm, while HT-WT only partially aggregated under the same conditions displaying a biphasic FCS trace, which represents putative monomers and larger aggregates (the predicted Rh of a globular 26-kDa HT of 2.9 nm agrees with the FSC-measured monomer size of 2-3 nm, Fig. 1b & c, consistent with[13]). Further, we observed an increase in the solvatochromic fluorophore's fluorescence lifetime attached to aggregating probe species (Fig. 1d & e). The native HT-aggr and HT-WT showed a unimodal distribution of lifetimes peaking at ~3.3 ns that broadened and shifted upon heating to longer lifetime values with a jagged plateau between 4.9 and 7.6 ns for HT-aggr (Fig. 1d) and two distinct peaks for HT-WT (Fig. 1e) corresponding to monomers and large aggregates, apparent in the FCS traces (Fig. 1c). This equivalence between the probe's fluorescence lifetime and aggregations state (Fig. 1a) provides means for monitoring the state of the aggregation probe in live cells by Fluorescence Lifetime Imaging Microscopy (FLIM). This methodology offers an accurate and absolute measure of the probe's state, free from the confounding effects of intensity calibrations and photo-bleaching[14,15,16], thus removing the limits associated with the intensity-based readouts.

Based on the probe's *in-vitro* performance, we sought to establish FLIM-based measurements of its folding/aggregation status in live cells. Consistent with the *in-vitro* measurements, heat-stress triggered aggregation of HT-aggr, transiently expressed in the cytoplasm or ER, as registered by an increase in probes' fluorescence lifetime (Fig. 1f-g). In line with previous observations[11,17], the ER appeared more resilient than the cytoplasm in maintaining HT-aggr soluble in heat-shocked cells, as reflected by an attenuated shift towards longer fluorescence lifetime in the ER, compared to cytoplasm-resident probe. Notably, the increase in fluorescence lifetime of the ER-targeted probe upon heat shock is considerably more heterogeneous in magnitude across the cell population than that of the cytoplasmic probe (Fig. 1 h). This points to greater resilience of the ER to protein aggregation in some cells (compare HT-aggr$^{ER}$ to HT-aggr$^{cyto}$ in Fig. 1h, note the presence of more/less heat-sensitive HT-aggr$^{ER}$ cells reflected in their yellow/green FLIM-appearance, respectively).

Prolonged expression of the probe in the ER led to spontaneous HT-aggr aggregation with an accumulation of large aggregate particles (apparent as red puncta - lifetime >5 ns, similar to the aggregates' values *in vitro,* Fig. 2a). Notably, the population of pixels with regular (non-punctate) ER-pattern also showed a longer lifetime (pixels in the yellow spectrum), presumably reflecting smaller sub-diffraction limit aggregation intermediates/oligomers mixed with native probe (mixture of green and red, Fig. 2a & b). The fraction of cells with FLIM-detectable aggregates (red puncta) increased with time up

bioRxiv preprint doi: https://doi.org/10.1101/2021.05.09.442953; this version posted May 9, 2021. The copyright holder for this preprint (which was not certified by peer review) is the author/funder, who has granted bioRxiv a license to display the preprint in perpetuity. It is made available under aCC-BY-NC-ND 4.0 International license.

to 9 days (Fig. 2c). From that point on, the size distribution of the aggregates drifted with time towards larger particles (Fig. 2d), indicating a further accumulation of aggregated material.

To establish whether the aggregated species accumulate in the ER lumen or post-retro-translocated into the cytoplasm, we implemented the Lightening super-resolution approach coupled to 3D FLIM enabled through a considerable improvement in the speed of the time-correlated single-photon counting of this modality[18]. Both the large, puncta-like aggregates (lifetime range in red) and the intermediates (lifetime range in yellow) showed a complete intra-ER localisation in the high-resolution fast 3D FLIM (Fig. 2e, video S1 in 3D). Further, the extent of intracellular aggregation of the HT-aggr variants (cell area fraction occupied by aggregates) correlated linearly with their unfolding equilibrium constant, a measure of their unfolding fraction [19] (Fig. 2 f-h). The differences in thermodynamic stability of HT-aggr variants explain the degree of aggregation-propensity of the HT-aggr variants Fig. 2h, inset). The properties of HT-aggr K73T suggest it as a useful variant for monitoring the capacity of the cellular protein folding quality control: This milder aggregation-prone probe showed expression levels at a steady-state similar to HT-WT (video S2 for HT-aggr K73T and S3 for HT-WT), and a relatively low, but detectable ER aggregates' load. Thus, FLIM of HT-aggr provides a space/time-resolved measure of aggregation in live cells, revealing that the chaperone-rich ER is not immune to protein aggregation – unfolded/misfolded intermediates of a metastable substrate may evade the folding quality control system accumulating over time in sizeable intra-ER aggregate particles.

The unfolded/misfolded intermediates of the probes and the aggregates that they give rise to were well tolerated with no cost to cell proliferation rates (Fig. 2i) and did not trigger a measurable increase in UPR activity at any point of the aggregate accumulation period (Fig. S2). Surprisingly, imposing ER stress pharmacologically did not increase the aggregated fraction of the probe (Fig. 3). In these experiments, we pulse-labelled the probe with its fluorescent reporter-ligand and chased the fate of its labelled sub-population over time in the presence or absence of various treatments (i.e., stress inducers, degradation blockers). This mode allows dissecting the aggregation, disaggregation and degradation events which the model protein is undergoing. Strikingly, ER stress induction decreased the intra-ER aggregation: a pulse-labelled population of HT-aggr$^{ER}$ showed a substantial shortening of fluorescence lifetime (Fig. 3a, b), and its aggregated fraction substantially reduced in a time-dependent manner following the induction of unfolded protein stress, through the inhibition of nascent proteins' N-glycosylation by tunicamycin (Tm, Fig. 3c, d, see ER stress markers' induction in Fig. S2). The diminished aggregation load manifested in a lower percentage of cells that show large puncta-like aggregate particles (lifetime > 5 ns, stand out as red colour coded pixels, Fig. 3a, c), and shrinking of the area occupied by these large aggregates (Fig. 3d). Moreover, in the FLIM images of tunicamycin treated cells, the entire distribution of pixels' fluorescence lifetime gradually shifted towards lower values in nearly all the cells (Fig. 3b). This indicates that the longer lifetime oligomeric intermediates of the probe (too small to be detected as puncta) are also cleared. A similar effect was observed for the most aggregation-prone HT-aggr variant M21K-F86L (Fig. S3).

bioRxiv preprint doi: https://doi.org/10.1101/2021.05.09.442953; this version posted May 9, 2021. The copyright holder for this preprint (which was not certified by peer review) is the author/funder, who has granted bioRxiv a license to display the preprint in perpetuity. It is made available under aCC-BY-NC-ND 4.0 International license.

Further, the probe faced a similar fate in human cortical neurons derived from induced pluripotent stem cells (iPSC): in these cells, too, HT-aggr$^{ER}$ formed puncta-like aggregates with a longer lifetime, whilst ER stress induction by tunicamycin lowered the aggregation load (Fig. S4).

Next, we examined the same aggregation parameters in cells prior and after induction of ER stress by other means – depleting ER calcium through its SERCA-ATP-ase pumps inhibition by thapsigargin. The aggregates clearance in these ER stress conditions was also evident through a shift of probe's fluorescence lifetime pixel distributions towards shorter values, decreased fractions of cells with aggregates and a contraction of the cell area occupied by aggregates (Fig. 3e-h).

The surprising effect of imposed ER stress on the abundance of the probe's aggregated fraction explainable by the activation of mechanisms that enhanced protein degradation by autophagosomal/lysosomal machinery or by a disaggregation activity in the ER (hitherto unknown). Presumably, proteasome-mediated elimination of the ER-aggregated probe should also require its disaggregation prior to retro-translocation to the cytoplasm, where proteasomes reside.

To distinguish between the two scenarios, we first investigated the turnover of HT-aggr$^{ER}$ under non-stress and stress conditions. The ER quality control machinery attends to the misfolding-prone substrates – it lowers the variants' expression by increasing their turnover (Table 1, Fig. S5, videos S2-S3). However, the induction of ER stress slowed down the degradation rates of the WT-HT and HT-aggr$^{ER}$ probes' variants (Table 1, Fig. S5, videos S4-S5). Besides, aggregate clearance evolved on a faster time scale than the probes' degradation in stress (Fig. 3, Table 1). Furthermore, the aggregate reduction effect of the ER stress was insensitive to autophagosomal/lysosomal blockers (Fig. S6). Therefore, the protein aggregation-antagonising effect of ER stress cannot be explained by enhanced autophagosomal/proteasomal degradation but consistent with the organelle's active disaggregation activity.

To this point, monitoring the fate of the HT-aggr$^{ER}$ reveals an inducible capability of the ER to resolve protein-aggregates formed from a fraction that eluded the organelle's quality control. This raises the question as to the identity of the ER disaggregation catalyst(s). In the cytoplasm, the chaperone network of Hsp100[20] (absent in metazoans) and Hsp70, fueled by ATP, can catalyse the solubilisation of protein aggregates[8–10]. Therefore, we hypothesised that the essential Hsp70-analogous ER chaperone BiP can be responsible for the organelle's disaggregation activity. BiP's candidacy for this role is further supported by its posttranslational/transcriptional response to ER stress, a condition in which we observe the disaggregation activity (Fig. 3). Namely, the UPR upscales BiP abundance and modulates its activity by amending the chaperone's posttranslational modification and oligomerisation status[21] prior to its upregulation and ER expansion.

Specific elimination of this key endogenous molecular chaperone by treating cells with Subtilase cytotoxin (SubAB) considerably augmented the probe's aggregated fraction (SubAB is a toxin from Shiga toxigenic strains of *E. coli* with a proteolytic A subunit that specifically targets BiP and B subunit responsible for internalisation and retrograde trafficking of the toxin to the ER[22], Fig. 4a-c). The aggregation-enhancing effect of SubAB

bioRxiv preprint doi: https://doi.org/10.1101/2021.05.09.442953; this version posted May 9, 2021. The copyright holder for this preprint (which was not certified by peer review) is the author/funder, who has granted bioRxiv a license to display the preprint in perpetuity. It is made available under aCC-BY-NC-ND 4.0 International license.

was exacerbated by stressing the ER with tunicamycin (Fig. 4a-c). These observations support the BiP's role in disaggregation. Further, they point to the significance of a balance in BiP quantity for native protein folding avoiding aggregation – through the increase in the levels of unfolded proteins (e.g. as a result of HT-aggr$^{ER}$ overexpression) is successfully offset by an increase in BiP, restoring/preserving homeostasis, its elimination cannot be thus be offset.

To further ascertain BiP's capacity to facilitate disaggregation, we sought to reconstruct this reaction *in vitro*. Since J-Domain proteins (DnaJs/ERdjs) modulate HSP70/BiP activity and are crucial for recruiting the chaperone to its substrates, we fused the HT aggregation probe to a minimal generic J-Domain (HT-aggr-JD). The JD fused to HT-aggr appeared functional as it recruited BiP and interfered with BiP's ATP-induced oligomerisation[23], unlike HT-aggr without JD (Fig. 4d). Critically, the tendency to form aggregates upon mild heating was preserved in the HT-aggr-JD fusion (Fig. 4e). A heat ramp traced by static light scattering showed that incubation at 53°C suffices to drive aggregation of HT-aggr-JD to completion (Fig. S7a, Fig. 4e red trace). Based on these, we presumed that aggregated HT-aggr-JD, with its J-domain *in cis,* can allow observing the chaperone's capacity, if it exists, as a disaggregase core.

Indeed, the aggregated fraction of the probe attracted BiP WT but not its substrate-binding deficient mutant (BiP V461F, Fig. 4f, reflected in a higher absorbance peak of the aggregated fraction in the presence of BiP WT). Conspicuously, the aggregation fraction of the mixture diminished over time in favour of low molecular weight species (Fig. 4g). To unmix HT-aggr-JD aggregations status in the BiP/substrate mixture, we monitored the probe through its ligand's fluorescence. Consistently with the UV-absorbance readings, this showed a BiP/ATP and time-dependent shift from aggregates towards smaller species (Fig. 4h). In the absence of BiP, or if the chaperone's ATP-fuelling is not provided, the aggregates not only remain stable but continue growing to a point where they are too large to pass the chromatography filter (Fig. 4i & S7b) but readily detectable by dynamic light scattering analysis (Fig. 4i, inset). These results indicate that ATP-fuelled BiP is capable of unravelling pre-formed protein aggregates. It is worth noting that the *in-vitro* measurements do not recapitulate the kinetics of this process accurately as BiP-assisting machinery is challenging to represent in all its complexity.

Collectively, the findings of the current study reveal that the ER stress response program contains the arm of inducible disaggregation. This complements its ability to preserve proteostasis by enhancing folding and reducing the load of client proteins (by chaperone expansion and attenuated protein synthesis/increased degradation, respectively). The three-layered PN response explains the organelle's ability to maintain high fidelity protein manufacturing inducing disaggregation in a space crowded with nascent/folding species.

Though one cannot exclude a possibility of additional disaggregases' involvement, the BiP system appears the only know ER-resident molecular machine with such a potential. Mechanisms of BiP repurposing from a holdase/foldase-like chaperone to a disaggrease may hold clues to identifying strategies for antagonising toxic aggregates/seeds that evade the unstressed system (e.g., A-beta oligomers[24]).

bioRxiv preprint doi: https://doi.org/10.1101/2021.05.09.442953; this version posted May 9, 2021. The copyright holder for this preprint (which was not certified by peer review) is the author/funder, who has granted bioRxiv a license to display the preprint in perpetuity. It is made available under aCC-BY-NC-ND 4.0 International license.

## Acknowledgements:

We are extremely grateful to David Ron and Steffen Preissler for their insights and advise of in-vitro chaperone studies and generous gifts of BiP vectors. We are also grateful to Paul McCormick, UK Leica Microsystems for invaluable technical support. This work is supported by grants for the UK Dementia Research Institute, which receives its funding from UK DRI Ltd, funded by the UK Medical Research Council, Alzheimer's Society and Alzheimer's Research UK and Alzheimer's Society (AS-595) to EA, from Portuguese national funds, FCT - Foundation for Science and Technology through project UID/Multi/04326/2019, from the operational programs CRESC Algarve 2020 and COMPETE 2020 through project EMBRC.PT ALG-01-0145-FEDER-022121 to EPM.

bioRxiv preprint doi: https://doi.org/10.1101/2021.05.09.442953; this version posted May 9, 2021. The copyright holder for this preprint (which was not certified by peer review) is the author/funder, who has granted bioRxiv a license to display the preprint in perpetuity. It is made available under aCC-BY-NC-ND 4.0 International license.

## References:

1. Anfinsen, C. B. Principles that Govern the Folding of Protein Chains. *Science* **181**, 223–230 (1973).

2. Ghosh, D. K. & Ranjan, A. The metastable states of proteins. *Protein Sci Publ Protein Soc* **29**, 1559–1568 (2020).

3. Balchin, D., Hayer-Hartl, M. & Hartl, F. U. Recent advances in understanding catalysis of protein folding by molecular chaperones. *Febs Lett* (2020) doi:10.1002/1873-3468.13844.

4. Hipp, M. S., Kasturi, P. & Hartl, F. U. The proteostasis network and its decline in ageing. *Nat Rev Mol Cell Biology* **20**, 421–435 (2019).

5. Walter, P. & Ron, D. The unfolded protein response: from stress pathway to homeostatic regulation. *Sci New York N Y* **334**, 1081–6 (2011).

6. Chambers, J. E., Petrova, K., Tomba, G., Vendruscolo, M. & Ron, D. ADP ribosylation adapts an ER chaperone response to short-term fluctuations in unfolded protein load. *J Cell Biology* **198**, 371–385 (2012).

7. Iadanza, M. G., Jackson, M. P., Hewitt, E. W., Ranson, N. A. & Radford, S. E. A new era for understanding amyloid structures and disease. *Nat Rev Mol Cell Biology* **19**, 755–773 (2018).

8. Nillegoda, N. B. *et al.* Crucial HSP70 co-chaperone complex unlocks metazoan protein disaggregation. *Nature* **524**, 247–251 (2015).

9. Faust, O. *et al.* HSP40 proteins use class-specific regulation to drive HSP70 functional diversity. *Nature* 1–6 (2020) doi:10.1038/s41586-020-2906-4.

10. Wentink, A. S. *et al.* Molecular dissection of amyloid disaggregation by human HSP70. *Nature* 1–6 (2020) doi:10.1038/s41586-020-2904-6.

11. Vincenz-Donnelly, L. *et al.* High capacity of the endoplasmic reticulum to prevent secretion and aggregation of amyloidogenic proteins. *Embo J* **37**, 337–350 (2018).

12. Liu, Y. *et al.* AgHalo: A Facile Fluorogenic Sensor to Detect Drug-Induced Proteome Stress. *Angewandte Chemie Int Ed* **56**, 8672–8676 (2017).

13. Rosa, A. M. M., Prazeres, D. M. F. & Paulo, P. M. R. Fluorescence correlation spectroscopy study of the complexation of DNA hybrids, IgG antibody, and a chimeric

bioRxiv preprint doi: https://doi.org/10.1101/2021.05.09.442953; this version posted May 9, 2021. The copyright holder for this preprint (which was not certified by peer review) is the author/funder, who has granted bioRxiv a license to display the preprint in perpetuity. It is made available under aCC-BY-NC-ND 4.0 International license.

protein of IgG-binding ZZ domains fused with a carbohydrate binding module. *Phys Chem Chem Phys Pccp* **19**, 16606–16614 (2017).

14. Lakowicz, J. R. *Principles of Fluorescence Spectroscopy*. (2006). doi:10.1007/978-0-387-46312-4_8.

15. BECKER, W. Fluorescence lifetime imaging - techniques and applications: FLUORESCENCE LIFETIME IMAGING. *J Microsc-oxford* **247**, 119–136 (2012).

16. Avezov, E. *et al.* Lifetime imaging of a fluorescent protein sensor reveals surprising stability of ER thiol redox. *J Cell Biology* **201**, 337–49 (2013).

17. Rousseau, E. *et al.* Targeting expression of expanded polyglutamine proteins to the endoplasmic reticulum or mitochondria prevents their aggregation. *Proc National Acad Sci* **101**, 9648–9653 (2004).

18. Alvarez[1], L. A. J. *et al.* SP8 FALCON: a novel concept in fluorescence lifetime imaging enabling video-rate confocal FLIM. *NATURE METHODS* (2019).

19. Estrela, N. *et al.* Sucrose prevents protein fibrillation through compaction of the tertiary structure but hardly affects the secondary structure. *Proteins* **83**, 2039–51 (2015).

20. Glover, J. R. & Lindquist, S. Hsp104, Hsp70, and Hsp40. *Cell* **94**, 73–82 (1998).

21. Preissler, S. & Ron, D. Early Events in the Endoplasmic Reticulum Unfolded Protein Response. *Csh Perspect Biol* **11**, a033894 (2018).

22. Paton, A. W. *et al.* AB5 subtilase cytotoxin inactivates the endoplasmic reticulum chaperone BiP. *Nature* **443**, 548–552 (2006).

23. Preissler, S. *et al.* AMPylation targets the rate-limiting step of BiP's ATPase cycle for its functional inactivation. *Elife* **6**, e29428 (2017).

24. Meli, G. *et al.* Conformational targeting of intracellular Aβ oligomers demonstrates their pathological oligomerization inside the endoplasmic reticulum. *Nat Commun* **5**, 3867 (2014).

25. Fernandopulle, M. S. *et al.* Transcription Factor-Mediated Differentiation of Human iPSCs into Neurons. *Curr Protoc Cell Biology* **79**, e51 (2018).

26. Chaumont, F. de *et al.* Icy: an open bioimage informatics platform for extended reproducible research. *Nat Methods* **9**, 690–6 (2012).

bioRxiv preprint doi: https://doi.org/10.1101/2021.05.09.442953; this version posted May 9, 2021. The copyright holder for this preprint (which was not certified by peer review) is the author/funder, who has granted bioRxiv a license to display the preprint in perpetuity. It is made available under aCC-BY-NC-ND 4.0 International license.

27. Sekine, Y. *et al.* Mutations in a translation initiation factor identify the target of a memory-enhancing compound. *Science* **348**, 1027–1030 (2015).

28. Paton, A. W., Srimanote, P., Talbot, U. M., Wang, H. & Paton, J. C. A New Family of Potent AB5 Cytotoxins Produced by Shiga Toxigenic Escherichia coli. *J Exp Medicine* **200**, 35–46 (2004).

29. Fares, M. *et al.* A Molecular Rotor-Based Halo-Tag Ligand Enables a Fluorogenic Proteome Stress Sensor to Detect Protein Misfolding in Mildly Stressed Proteome. *Bioconjugate Chem* **29**, 215–224 (2018).

30. Liu, Y. *et al.* A HaloTag-Based Multicolor Fluorogenic Sensor Visualizes and Quantifies Proteome Stress in Live Cells Using Solvatochromic and Molecular Rotor-Based Fluorophores. *Biochemistry-us* **57**, 4663–4674 (2018).

31. Holcman, D. *et al.* Single particle trajectories reveal active endoplasmic reticulum luminal flow. *Nat Cell Biol* **20**, 1118–1125 (2018).

bioRxiv preprint doi: https://doi.org/10.1101/2021.05.09.442953; this version posted May 9, 2021. The copyright holder for this preprint (which was not certified by peer review) is the author/funder, who has granted bioRxiv a license to display the preprint in perpetuity. It is made available under aCC-BY-NC-ND 4.0 International license.

# Methods:

## Cell culture and HT transfection

Monkey African green kidney cell line (COS7) and hamster Chinese ovary cell line (CHO-K1) were cultured in Dulbecco's Modified Eagle's medium (DMEM) supplemented with 10% fetal calf serum, 1% pen/strep (100 IU/mL and 100 $\mu$g/mL, respectively) and 1% L-glutamine (10mM). For human embryonic kidney 293 cells (HEK 293T), 2-Mercaptoethanol at 50 $\mu$M final concentration and non-essential amino acids (1:100) were used as additional supplements. Induced pluripotent stem cells (iPSC) were cultured as in[25]. Transient transfection of COS7 cells was performed using the Neon Transfection System (Invitrogen), applying 5 $\mu$g of plasmid per 1x10$^6$ cells. Stable CHO-K1 cell lines expressing HT WT and variants were obtained by retroviral infection. Retroviral particles were produced in HEK 293T cells using Transit IT transfection reagent (Mirus Bio) and plasmids SP_H6_Halo_pBABEpu (5 $\mu$g), pLVS-VG (1.5 $\mu$g), pJK3 (3 $\mu$g) and pCMV_TAT_HIV (0.6 $\mu$g) (see plasmids table in supplementary material). Cells were grown overnight at 37°C and then incubated at 32°C for 24 h in fresh media containing 1% BSA. Media containing the retroviral particles was collected, filtered through a 0.45 $\mu$m filter and stored at 4°C. Fresh media containing 1 % BSA was added to the cells kept at 32°C to collect the second batch of retroviral particles 24 h later. Recipient CHO-K1 cells 25 % confluent were incubated at 37°C with media containing retroviral particles diluted 1:2 in F12 media supplemented with 2 $\mu$g/mL of polybrene for around 12 h. After this period, cells were incubated in fresh media for 24 h before adding puromycin at 6 $\mu$g/mL. After 48 h, media was replaced, and puromycin concentration increased to 8 $\mu$g/mL for selection of stable expressors. Afterwards (24-48 h), cells were labelled with HT fluorescent ligand TMR (Promega) and sorted for stable HT expressors.

## Confocal microscopy, FLIM, fast 3D FLIM and image analysis

Cells were imaged in coverslips bottom dishes in complete medium with a laser confocal microscopy system (LSM 710, Carl Zeiss) equipped with an Argon laser and a Plan-Apo-chromat 60x oil immersion lens (NA 1.4) coupled to a microscope incubator, maintaining standard cell culture conditions. FLIM images were acquired with a time-correlated single-photon counting PicoQuant module coupled to the LSM 710 described above using a pulsed 440 nm diode laser for excitation, an MBS 405/485 nm dichroic and an emission filter of LP520. Instrument Response Function was recorded by light scattered on a clean coverslip. Fluorescence lifetimes and colour coded FLIM images were analysed with Sympho Time 64 PicoQuant software as in [16]. Fast 3D FLIM images were acquired on Falcon8 (Leica). Aggregate detection and quantitation were performed on the Icy platform[26]. For pulse-chase experiments on CHO-K1 HT stable expressors, cells were labelled with 4 $\mu$M P1 solvatochromic fluorophore [12] in PBS at 37°C for 45 min. After labelling, cells were washed with PBS, and fresh media was added to let cells recover for 1 hour before adding tunicamycin (0.5 $\mu$g/mL) or thapsigargin (0.5 $\mu$M) directly to the media when required. For the heat-shock of COS7 cells transiently transfected with HT, the same pulse-labelling was used, but a mixture of TMR (Promega) and P1 fluorophore (0.5 $\mu$M and 4 $\mu$M, respectively) in PBS was used instead of P1 alone as P1 is dim for

bioRxiv preprint doi: https://doi.org/10.1101/2021.05.09.442953; this version posted May 9, 2021. The copyright holder for this preprint (which was not certified by peer review) is the author/funder, who has granted bioRxiv a license to display the preprint in perpetuity. It is made available under aCC-BY-NC-ND 4.0 International license.

non-aggregated HT and TMR fluorescence allows spotting transfected cells. The heat shock was done by increasing the temperature to 43°C in the microscope incubator, and after reaching that temperature, a time-course of images was acquired

## Automated microscopy measurements: growth curves and HT turnover rates

CHO-K1stably expressing HTs were platted in a 6 well plate at low density ($5x10^4$ cells) and cell confluence imaged with the 10x objective every 4h using the phase-contrast channel of the Sartorius Incucyte live-cell imaging system (Göttingen, Germany). Exponential growth was fitted to the equation $\% conf_t = \% conf_{t0}\, 2^{(t/td)}$, where td is the time for a cell division (doubling time). To measure the turnover of HT, cells were platted at the same low density, grown overnight and then labelled with 0.25 $\mu$M TMR fluorophore (Promega) in media for 6h. After that, media was removed, cells washed with PBS, and fresh media added to start image the red fluorescence channel every 4h with the 10x objective. TMR fluorescence decay was fitted to an exponential decay using the equation $(\text{TMR Int. Intens.}_t/conf_t)=(\text{TMR Int. Intens.}_{t0}/conf_{t0})\, \exp^{(-kd/t)}$ where TMR Int. Intens. is the TMR integrated fluorescence intensity corresponding to the amount of HT labelled, conf is cell confluence, and $k_d$ is the HT degradation rate constant. Half-life times were calculated by $t_{1/2}=\ln 2/k_d$. TMR fluorescence needs to be divided by cell confluence to account for cell content sharing between daughter cells as doubling time is significantly faster than HT turnover for most variants and conditions.

## Flow cytometry

The effect of the Unfolded Protein Response was studied by a viral infection of CHO-K1 CHOP-GFP and Xbp1-MTurquoise reporters cell line[27] expressing HT-WT and HT-aggr. To identify the expressing cells, TMR labelling was performed. To evaluate whether the HT-aggr induces the UPR response, cells were analysed after infection for 48h, 72h, and then for 7 and 9 days. Where indicated, cells were treated with the ER stress-inducing agent tunicamycin (0.5 $\mu$M) for 24h to induce the UPR. Cells were analysed using four-channel CytoFLEX flow cytometer (Beckman Coulter), GFP (excitation laser 488nm, filter 525/40), M-Turquoise (excitation laser 405nm, filter 450/45) and TMR signals (excitation laser 561, filter 585/42) were detected. The data were processed using the FlowJo software (BD).

## Fluorescence correlation spectroscopy and static and dynamic light scattering

The FCS measurements were performed with a Microtime 200 setup from PicoQuant GmbH (Germany). The setup is equipped with a pulsed diode laser excitation source (LDH-P-C-485 PicoQuant, 482 nm, with a repetition rate of 20 MHz) coupled to an Olympus IX-71 inverted microscope. The laser beam was focused ~10 $\mu$m deep into the sample solution by a 60x water immersion objective with a numerical aperture of 1.2 (UPLSAPO 60XW, Olympus). Fluorescence was collected by the same objective and passed through a dichroic beam-splitter (485DRLP, Omega) to clean up the back-scattered light from laser excitation. The detected light is further selected by using a 510ALP long-pass filter (Omega). The collected light is then focused by a detection tube

bioRxiv preprint doi: https://doi.org/10.1101/2021.05.09.442953; this version posted May 9, 2021. The copyright holder for this preprint (which was not certified by peer review) is the author/funder, who has granted bioRxiv a license to display the preprint in perpetuity. It is made available under aCC-BY-NC-ND 4.0 International license.

lens to the 50 $\mu$m pinhole. The re-collimated beam is divided by means of a 50/50 non-polarising beam splitter cube and is detected by two single-photon avalanche diode detectors (SPCM-AQR-13, Perkin Elmer). Time-traces of fluorescence intensity from the two detectors were cross-correlate to avoid after-pulsing artefacts. The output signal was computer-processed by a TimeHarp 200 TCSPC card (PicoQuant). The focal area and the detection volume were calibrated at the beginning of each set of measurements using Atto655-COOH with an assumed diffusion coefficient, D, of 425 $\mu m^2/s$ in water at 25°C[13]. The autocorrelation curves were fitted with a pure diffusional model to determine the diffusion coefficient, which was then used to estimate the hydrodynamic radius Rh by the Stokes-Einstein equation [13]. The dynamic light scattering measurements were carried in a Zetasizer nano-ZS (Malvern), and the autocorrelation curves as a function of delay time were fitted to an exponential function using the Zetasizer software to extract the diffusion coefficient from which the hydrodynamic diameter Dh can be calculated by using the Stokes-Einstein equation. Static light scattering was carried out in a fluoromax-4 spectrofluorometer (Horiba Scientific), coupled to a water bath used to increase the temperature, using excitation and emission wavelengths of 500 nm.

## Protein purification

For in vitro assays, HT, HT-aggr fused to a J domain (HT-aggr-JD) and BiP were expressed in the *Escherichia coli* BL21 (DE3) strain, purified with Ni-nitrilotriacetic acid (NTA) affinity chromatography (HisTrap HP columns from GE Healthcare) in an AKTA purifier (GE Healthcare) and imidazole was removed by dialysis. Protein purity was checked by SDS-Page. SubAB was also purified as a His6-tagged fusion protein in *E. coli* BL21 (DE3) *lpxM*- and purified by Ni-NTA chromatography as previously described [28]

**Expression and purification of HT-WT and HT-aggr.** Detailed methods have been described in[29]. In brief, HT-WT or HT-aggr were encoded in pET29b plasmid with a c-terminal Histidine-6 tag. Cell cultures were carried out in LB and allowed to grow at 37°C until OD600 0.8. Protein expression was carried out by induction of 0.5 mM IPTG at 18°C overnight. Protein was purified on a BioRad Nuvia IMAC NiNTA column and subsequently a HiPrepTM 16/60 Sephacryl S-200 HR size-exclusion column. The protein containing fractions were identified by SDS-PAGE gel analysis, pooled, and concentrated. Purity of proteins was estimated using SDS-PAGE analyses to be > 98% based on SDS-PAGE.

**Urea-induced denaturation.** Purified WT-HT or HT-aggr (final concentration of 30 µM in PBS) were denatured in 8M urea for 30 min to achieve a complete denaturation. Denatured HT-WT or HT-aggr were mixed with folded HT-WT or HT-aggr to varying urea concentrations for a 12-h incubation. Protein denaturation was monitored by fluorescence emission spectra of tryptophan residues. Because tryptophan fluorescence exhibited a redshift from 330 nm to 355 nm in denatured HaloTag, the ratio of fluorescence intensity at 330 nm and 355 nm ($I_{330}/I_{355}$) was used to quantify the ratio of denatured versus folded HT. Fluorescence emission spectra were then collected using a Tecan infinite M1000Pro

bioRxiv preprint doi: https://doi.org/10.1101/2021.05.09.442953; this version posted May 9, 2021. The copyright holder for this preprint (which was not certified by peer review) is the author/funder, who has granted bioRxiv a license to display the preprint in perpetuity. It is made available under aCC-BY-NC-ND 4.0 International license.

microplate reader (ex = 280 nm). Fluorescence intensities of tryptophan at 330 nm and 355 nm were used for further analyses. Spectra at varying urea concentrations were collected and analysed in a similar fashion. All experiments were carried out at 25 ºC.

**Thermodynamic stability.** To determine thermodynamic stability, we used a two-state folding model wherein the Gibbs free energy of unfolding at a given urea concentration can be determined by Equation 1.

$$\Delta G^0 = -RTln(f_D/1 - f_D) \quad \text{(Eq. 1)}$$

where $f_D$ is the fraction of denatured protein, R = 8.314 J mol$^{-1}$ K$^{-1}$, T = 298 K. Subsequently, $\Delta G^0$ was plotted as a function of urea concentration to determine the thermodynamics of unfolding using Equation 2.

$$\Delta G^0_{urea} = \Delta G^0_{water} - m[urea] \quad \text{(Eq. 2)}$$

Where $\Delta G^0_{urea}$ is the $\Delta G^0$ at varying urea concentrations as determined by Eq. 1, [urea] is concentration of urea, $\Delta G^0_{water}$ is the Gibbs free energy of unfolding in water.

## Gel filtration chromatography and *in-vitro* HT (dis)aggregation assays

All the gel filtration chromatograms were ran in a Superdex 200 increase 10/300 column (fractionation range 10-600 kDa, GE Healthcare) coupled to an AKTA purifier, under isocratic elution in HKM buffer (Hepes 20 mM pH 7.4, NaCl 150 mM and $MgCl_2$ 10 mM). For the assays with aggregated HT-aggr-JD, firstly HT was labelled to 40% with the P2 solvatochromic fluorophore[30] and then protein aggregation was promoted by heating a 50 $\mu$M HT-aggr-JD solution to 53°C for 20 min. Aggregated HT-aggr-JD was then filtered (0.22 $\mu$m), mixed with the other components to final concentrations of 10 $\mu$M HT-aggr-JD, 9 mM ATP and 50 $\mu$M BiP and incubated on a rotating wheel at RT.

bioRxiv preprint doi: https://doi.org/10.1101/2021.05.09.442953; this version posted May 9, 2021. The copyright holder for this preprint (which was not certified by peer review) is the author/funder, who has granted bioRxiv a license to display the preprint in perpetuity. It is made available under aCC-BY-NC-ND 4.0 International license.

## Figure Legends:

**Fig. 1**. **Fluorescence lifetime-based probing system for real-time monitoring of protein aggregation. (a)** Schematic representation of the HT-aggr probing system. **(b)** Normalised autocorrelation function (G(τ)-1) from fluorescence correlation spectroscopy measurements of purified, native or heat-aggregated HT-aggr (K73T) probe or **(c)** HaloTag wild type (HT-WT), labelled with the solvatochromic fluorophore P1[12]. Solid lines represent best fits of the autocorrelation function considering a single species for HT-aggr and HT-WT, and two species for heat-aggregated HT-WT, as shown by the hydrodynamic radius values in the inset. **(d)** and **(e)** Fluorescence lifetime histograms of samples in (b) and (c), respectively. **(f)** A time series of live-cell fluorescence lifetime micrographs (FLIM) of HT-aggr (K73T) transiently expressed in the ER or cytoplasm of COS7 cells, before and after exposure to a heat shock treatment (43°C). **(g)** Fluorescence lifetime histograms from image-series shown in f. **(h)** fluorescence lifetime values of individual cells as in (f).

**Fig. 2 Intra-ER accumulation of non-toxic aggregates of the metastable HT-aggr.** (**a)** Time series of FLIM micrographs of CHO-K1 cells post stable transduction with ER targeted HT-aggr probe (K73T), labelled with P1 fluorophore. ER-targeting of HT as in[31] (**b)** Plot of mean fluorescence lifetime values of HT-aggr$^{ER}$/P1 for the time points in (a). **(c)** Plot of the percentage of cells with FLIM-detectable aggregates (lifetime >5 ns, apparent as red puncta) from image-series as in (a). **(d)** Frequency distribution of aggregates' sizes extracted from FLIM time-series as in (a) using the Aggregates Detector, Icy algorithm. Each data point in (b-c) represents a field of view with multiple

bioRxiv preprint doi: https://doi.org/10.1101/2021.05.09.442953; this version posted May 9, 2021. The copyright holder for this preprint (which was not certified by peer review) is the author/funder, who has granted bioRxiv a license to display the preprint in perpetuity. It is made available under aCC-BY-NC-ND 4.0 International license.

cells, with a total 180, 195, 250 and 280 cells analysed for 4, 7, 9 and 28 days, respectively, (pooled in d) **P<0.01, ****P<0.0001, unpaired T-test. **(e)** High-resolution fast 3D FLIM image projections of CHO-K1 cells with HT-aggr$^{ER}$/P1 (**f)** FLIM images of live CHO-K1 cells stably expressing HT-WT$^{ER}$ or HT-aggr$^{ER}$ variants with various degrees of metastability, as indicated by Gibbs free energy values of unfolding ($\Delta G^0_{Unf}$), (h) inset. **(g)** Plot of relative cell area occupied by FLIM-detected aggregates (lifetime >5 ns, red puncta) quantified for the HT-aggr variants from images as in (f), 60, 42, 55 and 45 cells were analysed for WT, K73T, L172Q and M21K F86L variants, respectively, *P<0.05, **P<0.01, unpaired T-test. (**h)** Plot of relative cell area with aggregates (a measure of aggregation from (g) for each variant) as a function of its metastability, represented by the equilibrium constant of unfolding, expresses as $K_{Unf}=\exp(-\Delta G^0_{Unf}/RT)$[19], where $\Delta G^0_{Unf}$ is the free energy of unfolding (inset). **(i)** Growth curves for CHO-K1 cells expressing the HT-aggr$^{ER}$ variants along with parental cells. Solid lines are the fits for the exponential growth according to the equation $\%\ conf_t = \%\ conf_{t0}\ 2^{(t/td)}$, where td is the doubling time. Individual values of td are shown in the inset.

**Fig 3. Pharmacological ER stress induction activates protein disaggregation machinery.** (**a)** and **(e)** FLIM images of live CHO-K1 cells stably expressing HT-aggr$^{ER}$, untreated or treated with tunicamycin (Tm at 0.5 $\mu$g/mL) or thapsigargin (Tg at 0.5 $\mu$M) for a time period post-pulse-labelling with the P1 fluorochrome as indicated. **(b)** and **(f)** Histograms representing frequency distribution of pixel fluorescence lifetime from image-series as in (a) and (e), note the shift towards shorter lifetime values post-treatment

bioRxiv preprint doi: https://doi.org/10.1101/2021.05.09.442953; this version posted May 9, 2021. The copyright holder for this preprint (which was not certified by peer review) is the author/funder, who has granted bioRxiv a license to display the preprint in perpetuity. It is made available under aCC-BY-NC-ND 4.0 International license.

(traces represent individual cells), **(c)** and **(g)** Quantitation of the relative number of cells with FLIM-detected aggregates in images as in (a) and (e). (**d)** and **(h)** Plots of relative cell area occupied by FLIM-detected aggregates (lifetime >5 ns, red puncta) in images as in (a) and (e). Data points represent images with 30-45 cells were each, *P<0.05; **P<0.01; ****P<0.001, unpaired T-test.

**Table 1.** Turnover of $HT^{ER}$ variants, labelled with tetramethyl-rhodamine Halotag ligand (TMR, 250 nM, 6h), following the label removal, the samples were chase-imaged in the absence or presence of an ER stressor, tunicamycin (Tm, 0.5 $\mu$g/mL). The time of the decrease of TMR fluorescence to 50 % of the initial intensity (half-life, $t_{1/2}$) was calculated from fitting the curves to an exponential decay function (Fig. S5, see methods for details).

**Fig 4. ATP-driven HT disaggregation by Bip.** **(a)** FLIM images of live CHO-K1 cells stably expressing HT-aggr (K73T), untreated, treated with subtilase cytotoxin AB (SubAB at 0.4 □g/mL) or with SubAB plus tunicamycin (Tm at 0.5 $\mu$g/mL) for 24h. (**b)** Quantification of the relative number of cells with FLIM-detected aggregates in images as in (a), calculated at least for 90 cells per sample. (**c**) Quantification of the fraction of the cell area occupied by aggregates in images as in (a). **P<0.01; ***P<0.001, unpaired T-test. **(d)** Protein absorbance traces (280 nm) of BiP WT (50 $\mu$M) alone, with native HT-aggr or native HT-aggr, fused to J-domain (JD, 10 $\mu$M), resolved by gel filtration chromatography (10-600 kDa fractionation range). **(e)** Traces as in (d) of native HT-aggr,

bioRxiv preprint doi: https://doi.org/10.1101/2021.05.09.442953; this version posted May 9, 2021. The copyright holder for this preprint (which was not certified by peer review) is the author/funder, who has granted bioRxiv a license to display the preprint in perpetuity. It is made available under aCC-BY-NC-ND 4.0 International license.

native HT-aggr-JD and heat-aggregated HT-aggr-JD (53°C, 20 min, 10 $\mu$M). **(f)**, Traces as in (d, e) of aggregated as in (e) HT-aggr-JD, incubated with BiP WT/ATP or BiP V461F/ATP, a substrate-binding deficient BiP mutant. Note the increase in the main peak of the aggregated HT-aggr-JD (pale red) upon the addition of BiP WT/ATP only, indicative of its recruitment to the aggregates. **(g)**, Traces as in (d, e) of aggregated as in (e) HT-aggr-JD, incubated with BiP WT/ATP for the indicated periods. **(h)** Fluorescence traces of chromatograms as in (g) this time exclusively detecting HT-aggr-JD (pre-aggregated) through the fluorescence of its P2-halo ligand label. **(i)** Fluorescence traces of chromatograms for the P2-labelled HT-aggr-JD (pre-aggregated) in the absence of BiP for the same time course as in (h). Fluorescence was measured for discrete data points, 0.3 mL each. Dynamic light scattering measurements showing the hydrodynamic diameter (Dh) of P2-labelled HT-aggr-JD (pre-aggregated) for the same time course were plotted in the inset to unveil the growth of the aggregates in the absence of BiP and explain why aggregates are retained in the pre-filter of the column leading to a decreased amount eluted over time. The measurements in (d-i) were performed in the presence of ATP (3-9 mM), which elutes at 20.2 mL, fractions omitted from the chromatogram.

bioRxiv preprint doi: https://doi.org/10.1101/2021.05.09.442953; this version posted May 9, 2021. The copyright holder for this preprint (which was not certified by peer review) is the author/funder, who has granted bioRxiv a license to display the preprint in perpetuity. It is made available under aCC-BY-NC-ND 4.0 International license.

## Supplemental figure legends:

**Fig. S1. Metastability measurements of the Halotag-based aggregation probes.** HT-WT or HT-aggr variants (30 $\mu$M) were denatured in varying urea concentrations, and the extent of denaturation was measured through tryptophan fluorescence emission. A two-state model where only the native and the unfolded state are populated was assumed, and the Gibbs free energy of unfolding ($\Delta G^0_{Unf}$=-RT ln $K_{Unf}$) at different urea concentrations within the transition region was plotted against urea concentration to determine the thermodynamic stability of HT in water at 25 ºC ($\Delta G^0_{urea} = \Delta G^0_{water} - m$ [urea]).

**Fig. S2**. **Flow Cytometry analysis of UPR upon protein aggregation in the ER. (a**) Scatter plots of green/blue fluorescence of S21 CHO cells expressing the UPR fluorescent reporters GFP-CHOP1 and m-Turquoise-XBP1, reflecting PERK and IRE1 pathways activation, respectively[27]. Untransfected (control, Ctrl), transfected with HT-WT$^{ER}$ or HT-aggr$^{ER}$, untreated or exposed to tunicamycin (0.5 $\mu$g/mL, 6 h). **(b**) Measurements of GFP-CHOP1 UPR reporter as in (a) with detection of red fluorescence emanating from TMR Halo Ligand, identifying cells transfected with HT-WT$^{ER}$ or HT-aggr$^{ER}$ (red quadrants). **(c**) Histograms of fluorescence signals from GFP-CHOP1 and m-Turquoise-XBP1 in untransfected cells and HT-WT$^{ER}$ or HT-aggr$^{ER}$ expressing TMR-positive (red quadrants in b) cells measured following expression periods corresponding to the beginning and peak of aggregates accumulation in the ER (Fig. 2), as indicated.

**Fig. S3. Aggregates from a highly aggregation-prone HT-aggr variant cleared under ER stress. (a)** FLIM images of live CHO-K1 cells stably expressing HT-aggr M21KF86L variant untreated and treated with Tm (0.5 $\mu$g/mL) for 5 h and 18h. **(b)** Plot shows the quantification of the cell area fraction covered with aggregates n >45 cells. *P<0.05, **P<0.01, unpaired T-test.

**Fig. S4. ER stress-induced disaggregation of HT-aggr$^{ER}$ in neurones.** FLIM micrographs of Induced Pluripotent Stem (iPS) cells-derived cortical neuronal monolayer stably expressing HT-agg$^{ER}$ labelled with TMR Halo Ligand or P1 fluorophore, untreated or treated with tunicamycin. Note the aggregation of the probe in longer lifetime regions (yellow, red, examples denoted by arrowheads).

**Fig. S5. Turnover rates of HT$^{ER}$ variants**. Source data for Table 1 (see Video S2-S5). Degradation rates of stably expressed HT variants after a pulse labelling with TMR in live CHO-K1 cells in the absence **(a)** or presence of tunicamycin (0.5 $\mu$g/mL) **(b)**. The time-dependent decay of TMR fluorescence (reflecting the amount of HTs) was fitted to an exponential decay using the equation (TMR Int. $Intens._t/conf_t$) = (TMR Int. $Intens._{t0}$ /$conf_{t0}$)

bioRxiv preprint doi: https://doi.org/10.1101/2021.05.09.442953; this version posted May 9, 2021. The copyright holder for this preprint (which was not certified by peer review) is the author/funder, who has granted bioRxiv a license to display the preprint in perpetuity. It is made available under aCC-BY-NC-ND 4.0 International license.

exp $^{(-kd\ t)}$ where TMR Int. Intens. is the TMR integrated fluorescence intensity, conf is cell confluence, and $k_d$ is the HT degradation rate constant.

**Fig. S6. The aggregates-antagonising effect of the ER stressors is insensitive to autophagosomal/lysosomal blockers. (a)** Plots of mean +/- SD of fluorescence lifetime values measured as in Fig. 2b, of cells treated with Tm (0.5 $\mu$g/ml) in the presence or absence of the autophagy inhibitor Bafilomacyn (100 nM) or **(b)** the lysosomal inhibitor Chloroquine (10 $\mu$M). Each data point represents a FLIM field of view with multiple cells, with n>290 cells. **P<0.01; ****P<0.001Unpaired T-test.

**Fig. S7. Aggregation of HT-agg-JD in vitro. (a)** Thermal induced aggregation of HT-aggr (K73T) fused to the J domain (HT-aggr-JD) measured by static light scattering at 500 nm to define the range of temperature where protein aggregation occurs. The onset of aggregation occurred at 43.4 ± 1.2°C as calculated from the linear extrapolation of the increase in static light scattering. Note, at 53°C HT-aggr is entirely aggregated (confirmed by gel filtration chromatography, see Fig. 4e. **(b)** Fluorescence traces of chromatograms for the P2-labelled HT-aggr-JD (pre-aggregated) in the presence of BiP but absence of ATP for the same time course as in Fig. 4 g-i. Fluorescence was measured for discrete data points, 0.3 mL each. Dynamic light scattering measurements showing the hydrodynamic diameter (Dh) of P2-labelled HT-aggr-JD (pre-aggregated) for the same time course were plotted in the inset to unveil the growth of the aggregates in the absence of ATP and explain why aggregates are retained in the pre-filter of the column leading to a decreased amount eluted over time.

Fig. 1

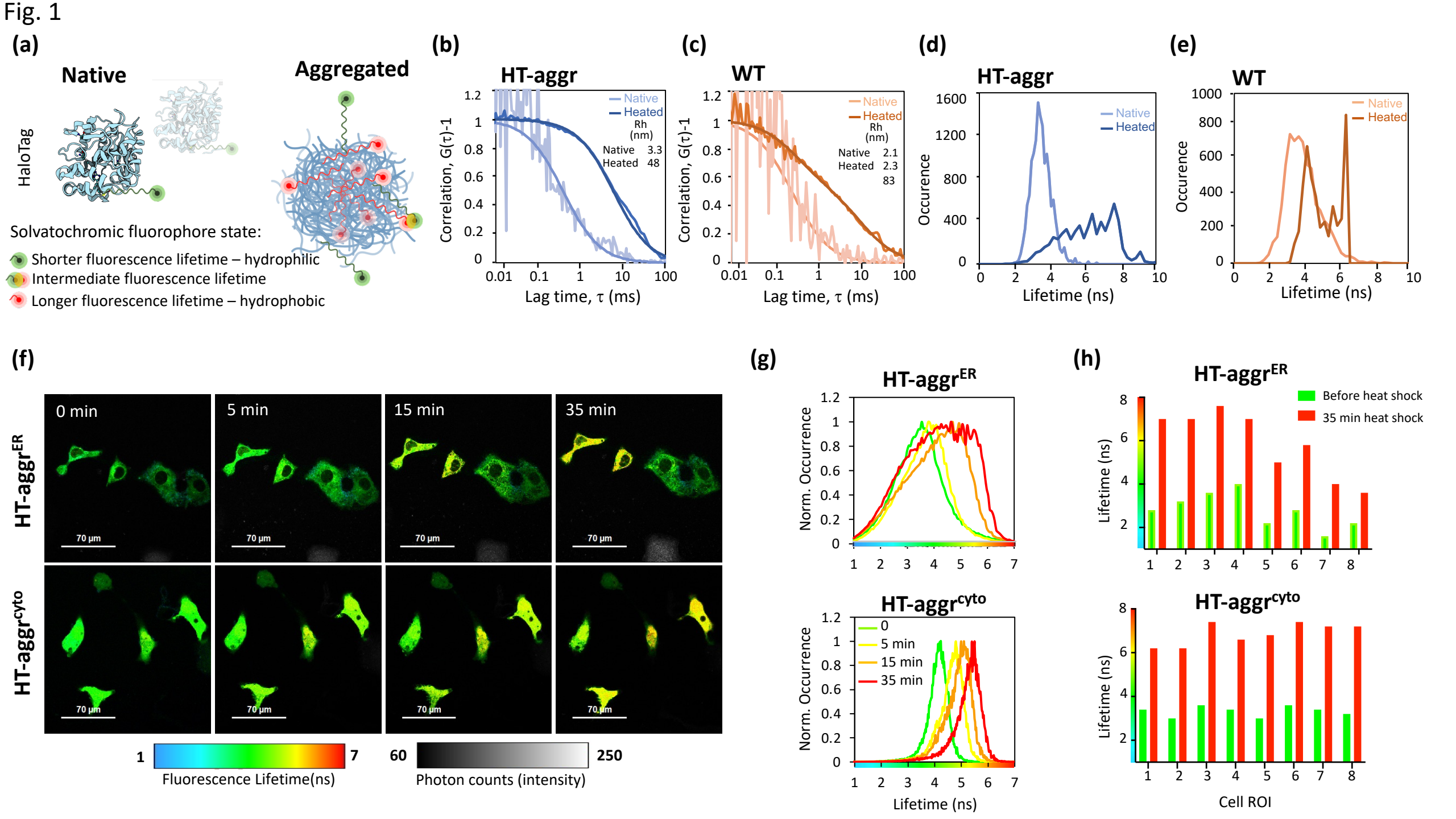
(a)
Native
Aggregated
HaloTag
Solvatochromic fluorophore state:
Shorter fluorescence lifetime – hydrophilic
Intermediate fluorescence lifetime
Longer fluorescence lifetime – hydrophobic
(b)
HT-aggr
Native
Heated
Rh (nm)
Native 3.3
Heated 48
Correlation, G(τ)-1
Lag time, τ (ms)
(c)
WT
Native
Heated
Rh (nm)
Native 2.1
Heated 2.3
83
Correlation, G(τ)-1
Lag time, τ (ms)
(d)
HT-aggr
Native
Heated
Occurence
Lifetime (ns)
(e)
WT
Native
Heated
Occurence
Lifetime (ns)
(f)
HT-aggrER
HT-aggrcyto
0 min
5 min
15 min
35 min
70 µm
1
7
Fluorescence Lifetime(ns)
60
250
Photon counts (intensity)
(g)
HT-aggrER
HT-aggrcyto
Norm. Occurrence
0
5 min
15 min
35 min
Lifetime (ns)
(h)
HT-aggrER
HT-aggrcyto
Before heat shock
35 min heat shock
Lifetime (ns)
Cell ROI

Fig. 2

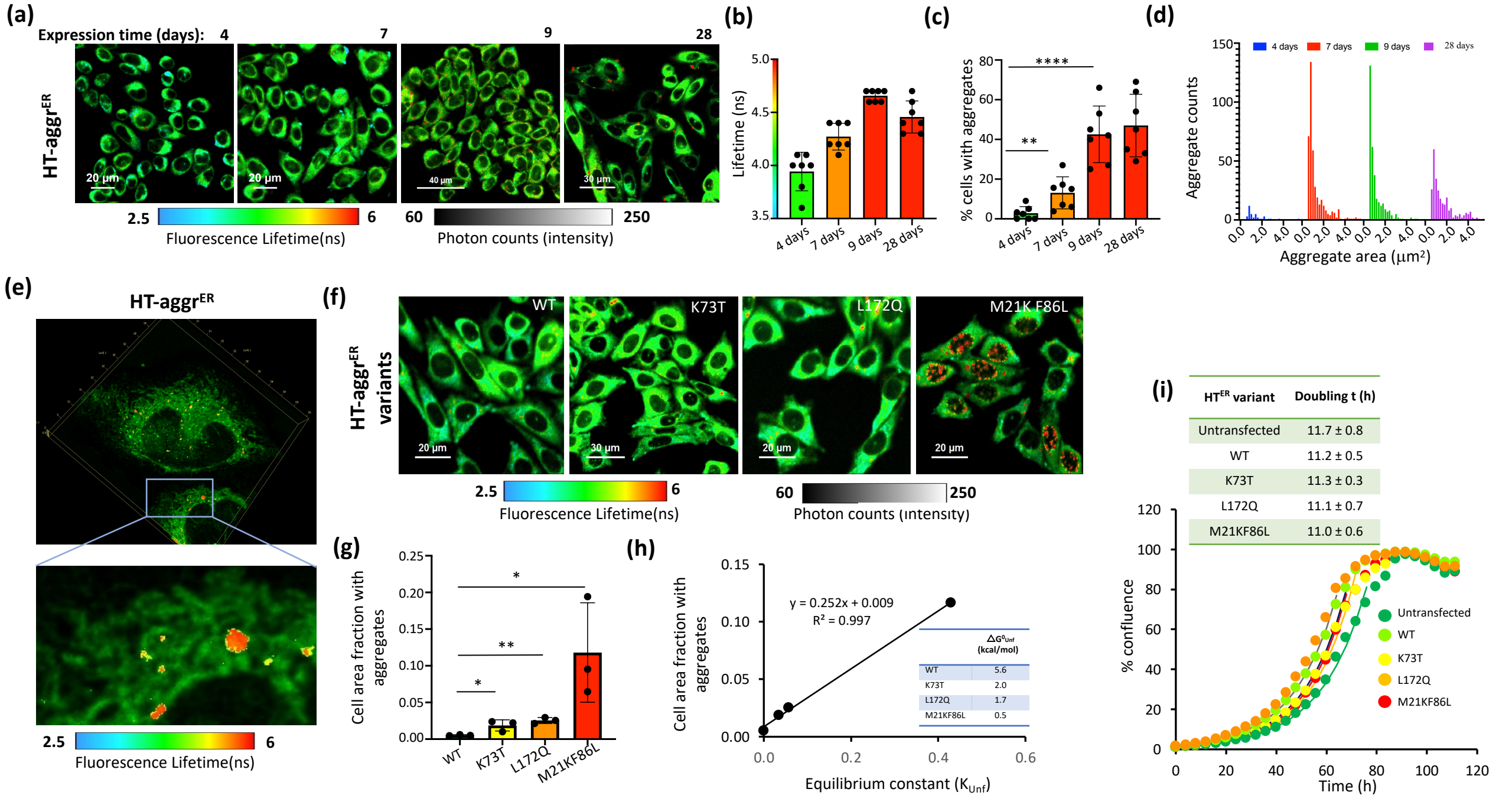
(a)
Expression time (days): 4 7 9 28
HT-aggr^ER
20 µm
20 µm
40 µm
30 µm
2.5
6
Fluorescence Lifetime(ns)
60
250
Photon counts (intensity)
(b)
Lifetime (ns)
5.0
4.5
4.0
3.5
4 days
7 days
9 days
28 days
(c)
% cells with aggregates
80
60
40
20
0
****
**
4 days
7 days
9 days
28 days
(d)
4 days
7 days
9 days
28 days
Aggregate counts
150
100
50
0
Aggregate area (µm²)
(e)
HT-aggr^ER
2.5
6
Fluorescence Lifetime(ns)
(f)
HT-aggr^ER variants
WT
K73T
L172Q
M21K F86L
20 µm
30 µm
20 µm
20 µm
2.5
6
Fluorescence Lifetime(ns)
60
250
Photon counts (intensity)
(g)
Cell area fraction with aggregates
0.25
0.20
0.15
0.10
0.05
0.00
*
**
*
WT
K73T
L172Q
M21KF86L
(h)
Cell area fraction with aggregates
0.15
0.10
0.05
0.00
y = 0.252x + 0.009
R² = 0.997
ΔG⁰Unf (kcal/mol)
WT 5.6
K73T 2.0
L172Q 1.7
M21KF86L 0.5
0.0
0.2
0.4
0.6
Equilibrium constant (KUnf)
(i)
HT^ER variant | Doubling t (h)
Untransfected | 11.7 ± 0.8
WT | 11.2 ± 0.5
K73T | 11.3 ± 0.3
L172Q | 11.1 ± 0.7
M21KF86L | 11.0 ± 0.6
% confluence
120
100
80
60
40
20
0
0
20
40
60
80
100
120
Time (h)
Untransfected
WT
K73T
L172Q
M21KF86L

Fig. 3

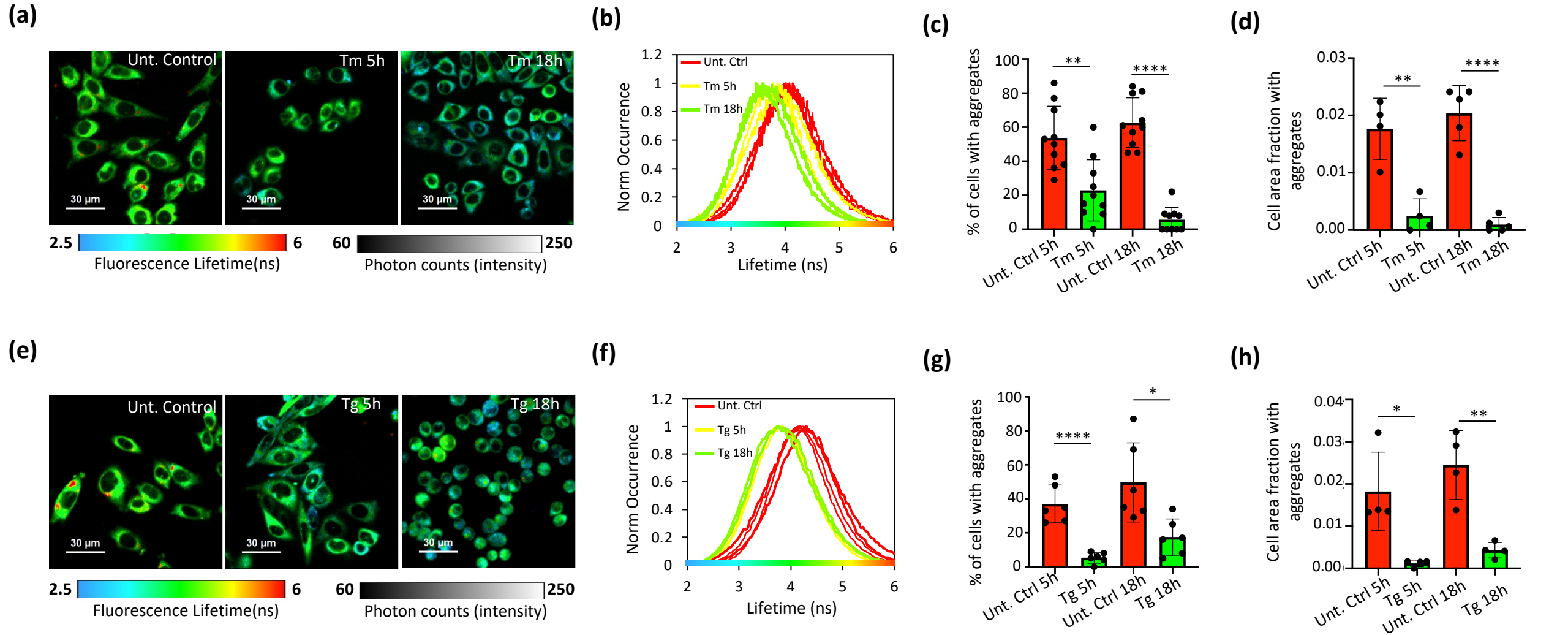
(a)
Unt. Control
Tm 5h
Tm 18h
30 µm
2.5
6
Fluorescence Lifetime(ns)
60
250
Photon counts (intensity)
(b)
Norm Occurrence
Unt. Ctrl
Tm 5h
Tm 18h
Lifetime (ns)
(c)
% of cells with aggregates
Unt. Ctrl 5h
Tm 5h
Unt. Ctrl 18h
Tm 18h
(d)
Cell area fraction with aggregates
(e)
Unt. Control
Tg 5h
Tg 18h
(f)
Tg 5h
Tg 18h
(g)
(h)

Table 1

HT$^{ER}$ variants degradation half-life time ($t_{1/2}$)

| HT$^{ER}$ variant | Untreated $t_{1/2}$ (hours) | $t_{1/2}$ in Tm-induced stress (hours) |
|---|---|---|
| **WT** | 41 ± 9 | 174 ± 21 |
| **K73T** | 32 ± 3 | 58 ± 7 |
| **L172Q** | 7 ± 2 | 27 ± 5 |
| **M21KF86L** | 28 ± 11 | 15 ± 3 |

Fig. 4

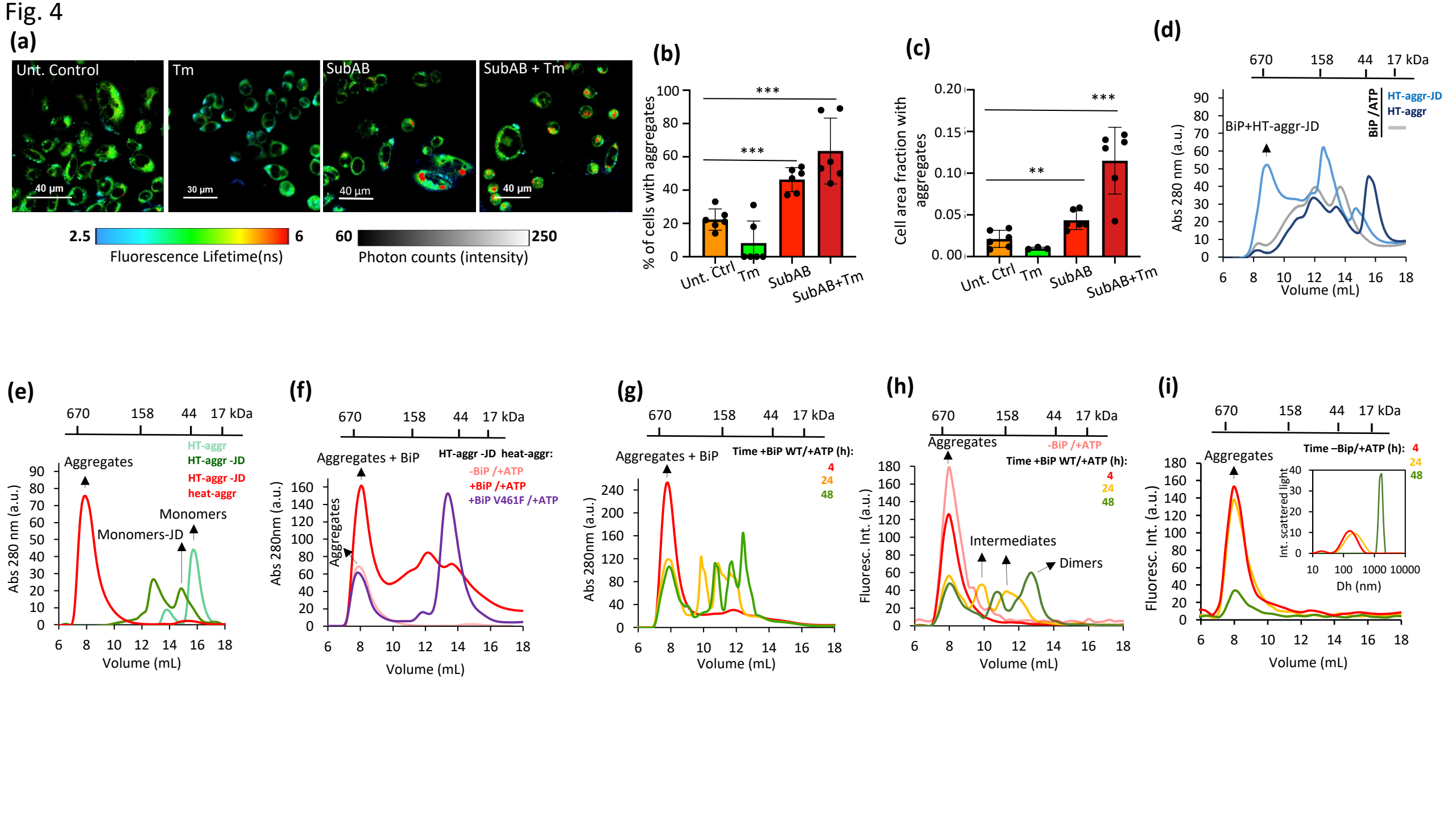
(a)
Unt. Control
Tm
SubAB
SubAB + Tm
40 µm
30 µm
40 µm
40 µm
2.5
6
Fluorescence Lifetime(ns)
60
250
Photon counts (intensity)
(b)
% of cells with aggregates
***
***
Unt. Ctrl
Tm
SubAB
SubAB+Tm
(c)
Cell area fraction with aggregates
***
**
Unt. Ctrl
Tm
SubAB
SubAB+Tm
(d)
670
158
44
17 kDa
BiP+HT-aggr-JD
BiP /ATP
HT-aggr-JD
HT-aggr
Abs 280 nm (a.u.)
Volume (mL)
(e)
670
158
44
17 kDa
HT-aggr
HT-aggr -JD
HT-aggr -JD
heat-aggr
Aggregates
Monomers
Monomers-JD
Abs 280 nm (a.u.)
Volume (mL)
(f)
670
158
44
17 kDa
Aggregates + BiP
HT-aggr -JD heat-aggr:
-BiP /+ATP
+BiP /+ATP
+BiP V461F /+ATP
Aggregates
Abs 280nm (a.u.)
Volume (mL)
(g)
670
158
44
17 kDa
Aggregates + BiP
Time +BiP WT/+ATP (h):
4
24
48
Abs 280nm (a.u.)
Volume (mL)
(h)
670
158
44
17 kDa
Aggregates
-BiP /+ATP
Time +BiP WT/+ATP (h):
4
24
48
Intermediates
Dimers
Fluoresc. Int. (a.u.)
Volume (mL)
(i)
670
158
44
17 kDa
Aggregates
Time –Bip/+ATP (h):
4
24
48
Int. scattered light
Dh (nm)
Fluoresc. Int. (a.u.)
Volume (mL)

Fig. S1

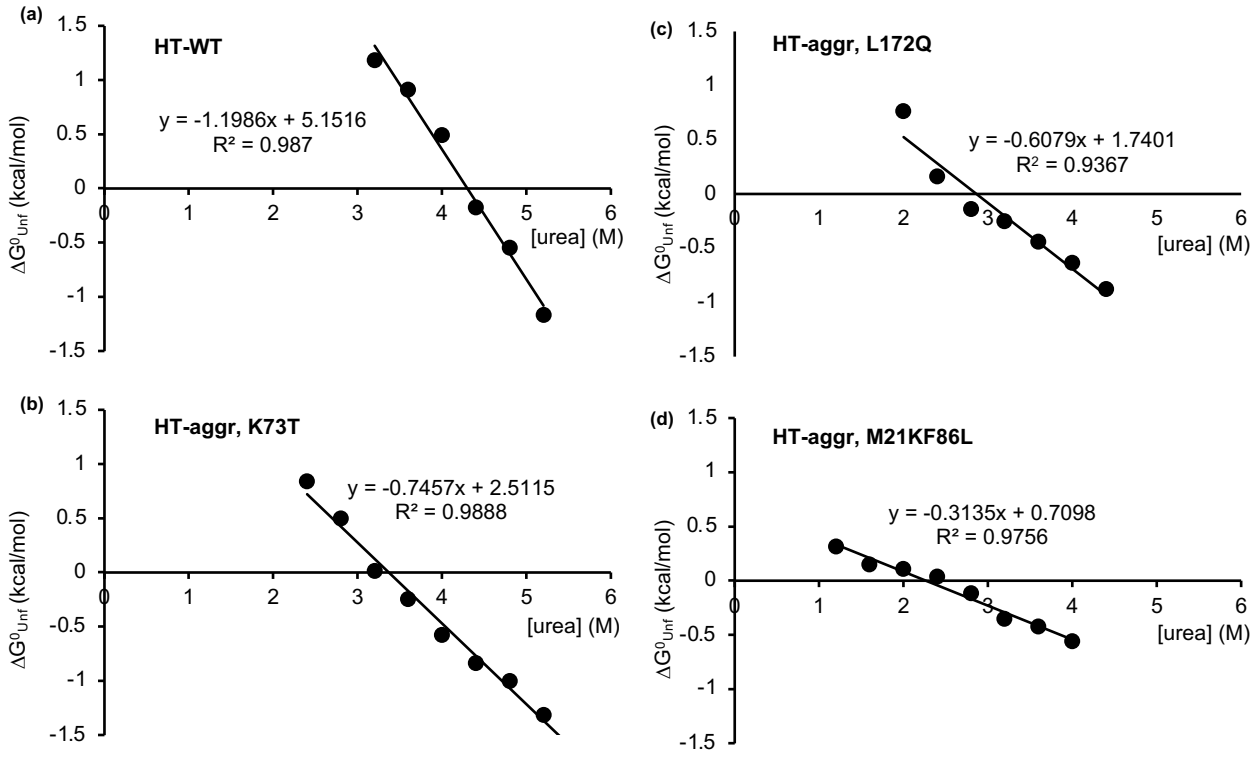
(a)
HT-WT
y = -1.1986x + 5.1516
R² = 0.987
(b)
HT-aggr, K73T
y = -0.7457x + 2.5115
R² = 0.9888
(c)
HT-aggr, L172Q
y = -0.6079x + 1.7401
R² = 0.9367
(d)
HT-aggr, M21KF86L
y = -0.3135x + 0.7098
R² = 0.9756
ΔG⁰Unf (kcal/mol)
[urea] (M)

Fig. S2

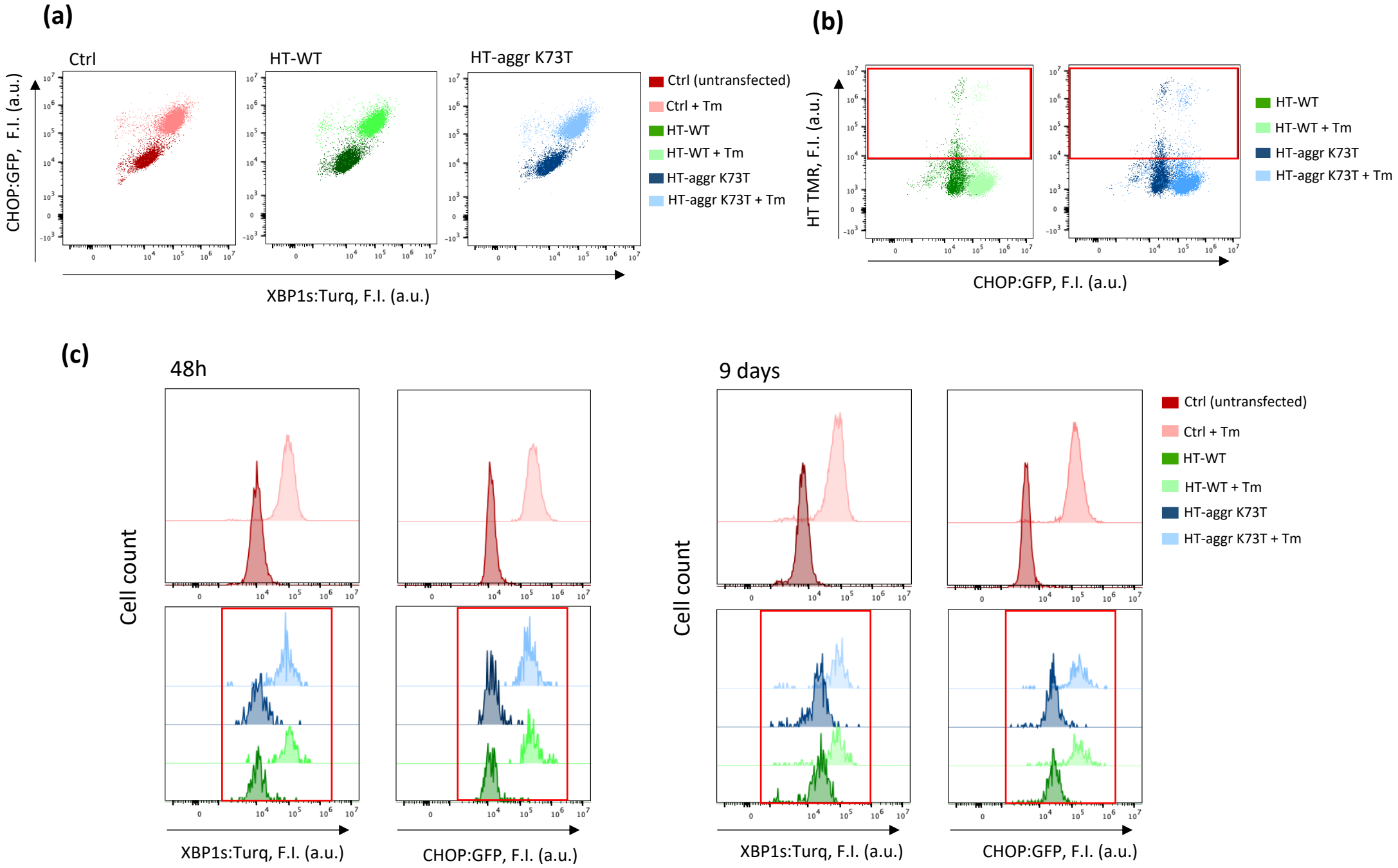
(a)
Ctrl
HT-WT
HT-aggr K73T
CHOP:GFP, F.I. (a.u.)
XBP1s:Turq, F.I. (a.u.)
Ctrl (untransfected)
Ctrl + Tm
HT-WT
HT-WT + Tm
HT-aggr K73T
HT-aggr K73T + Tm
(b)
HT TMR, F.I. (a.u.)
CHOP:GFP, F.I. (a.u.)
HT-WT
HT-WT + Tm
HT-aggr K73T
HT-aggr K73T + Tm
(c)
48h
9 days
Cell count
XBP1s:Turq, F.I. (a.u.)
CHOP:GFP, F.I. (a.u.)
Ctrl (untransfected)
Ctrl + Tm
HT-WT
HT-WT + Tm
HT-aggr K73T
HT-aggr K73T + Tm

Fig. S3

**(a)**

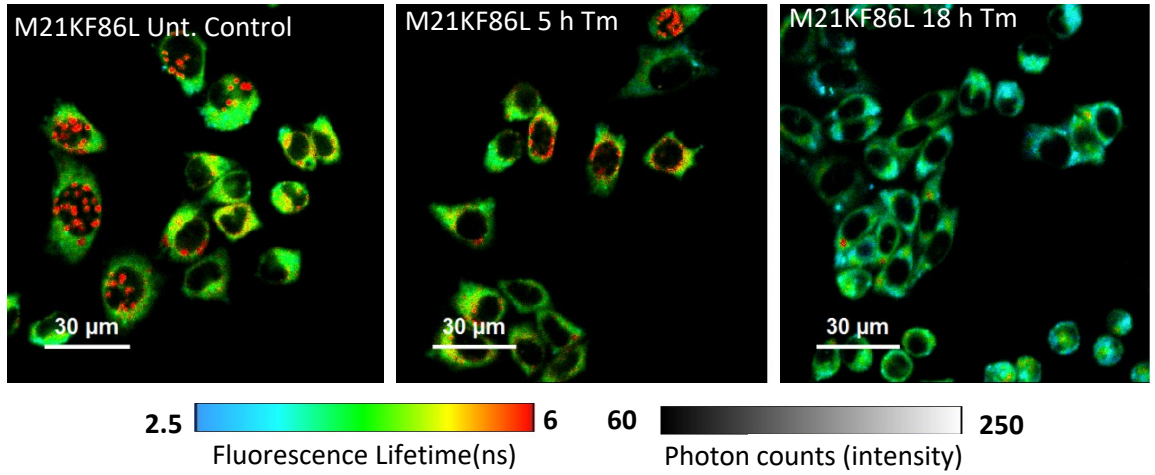
M21KF86L Unt. Control
M21KF86L 5 h Tm
M21KF86L 18 h Tm
30 µm
30 µm
30 µm
2.5
6
Fluorescence Lifetime(ns)
60
250
Photon counts (intensity)

**(b)**

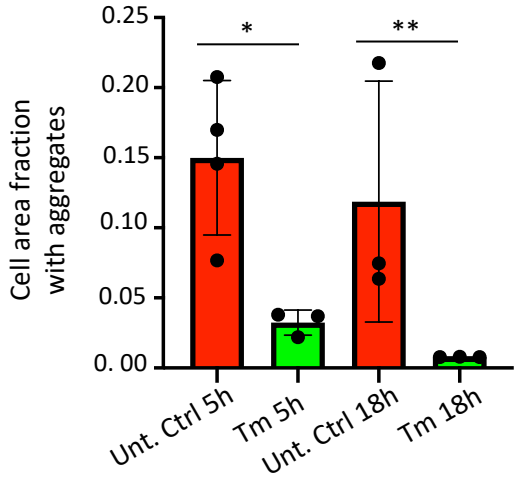
Cell area fraction with aggregates
0.25
0.20
0.15
0.10
0.05
0. 00
*
**
Unt. Ctrl 5h
Tm 5h
Unt. Ctrl 18h
Tm 18h

Fig. S4

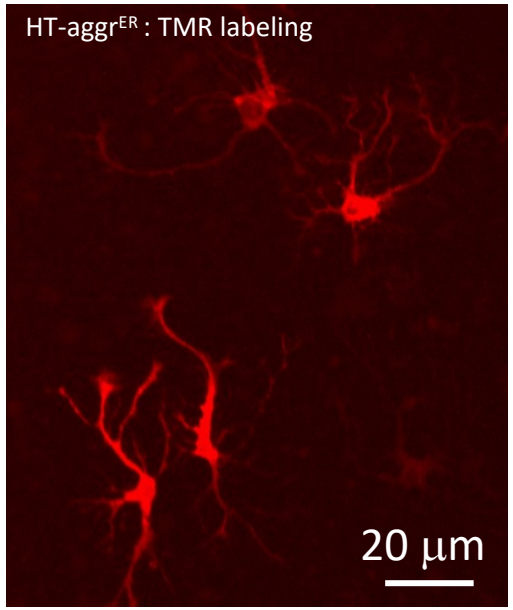
HT-aggr$^{ER}$ : TMR labeling
20 μm

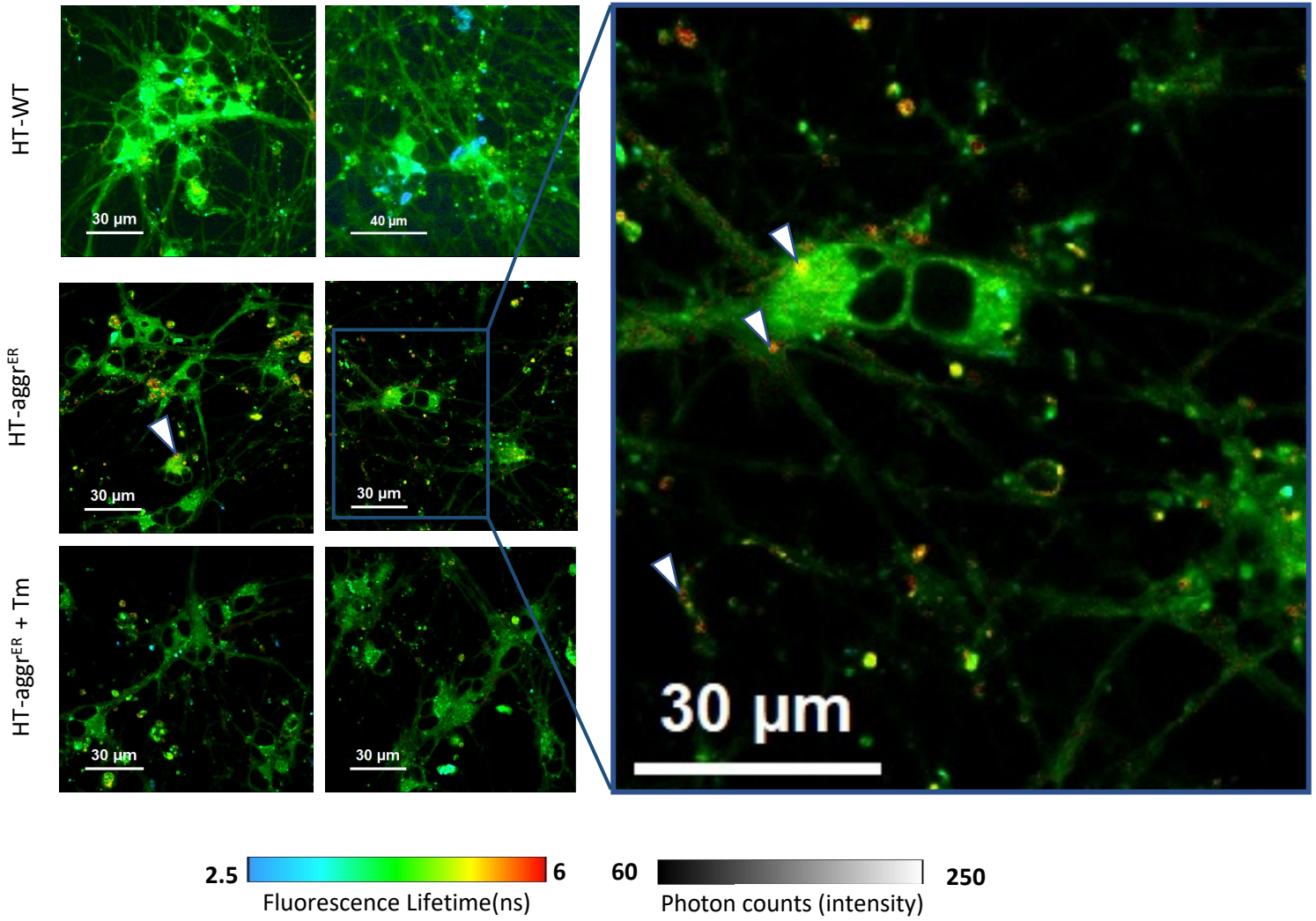
HT-WT
HT-aggr$^{ER}$
HT-aggr$^{ER}$ + Tm
30 μm
40 μm
30 μm
30 μm
30 μm
30 μm
30 μm
2.5
6
Fluorescence Lifetime(ns)
60
250
Photon counts (intensity)

Fig. S5

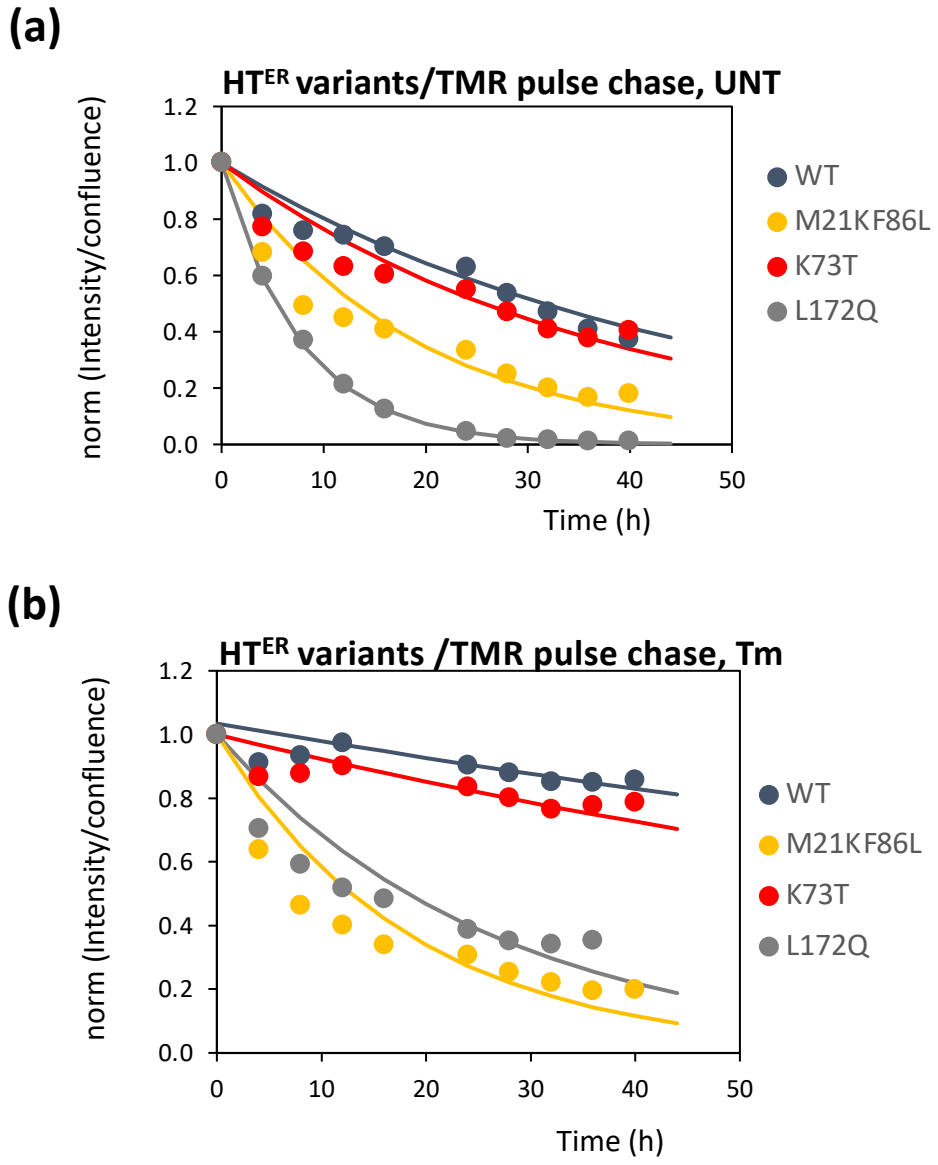
(a)
HTER variants/TMR pulse chase, UNT
norm (Intensity/confluence)
1.2
1.0
0.8
0.6
0.4
0.2
0.0
0
10
20
30
40
50
Time (h)
WT
M21KF86L
K73T
L172Q
(b)
HTER variants /TMR pulse chase, Tm
norm (Intensity/confluence)
1.2
1.0
0.8
0.6
0.4
0.2
0.0
0
10
20
30
40
50
Time (h)
WT
M21KF86L
K73T
L172Q

Fig. S6

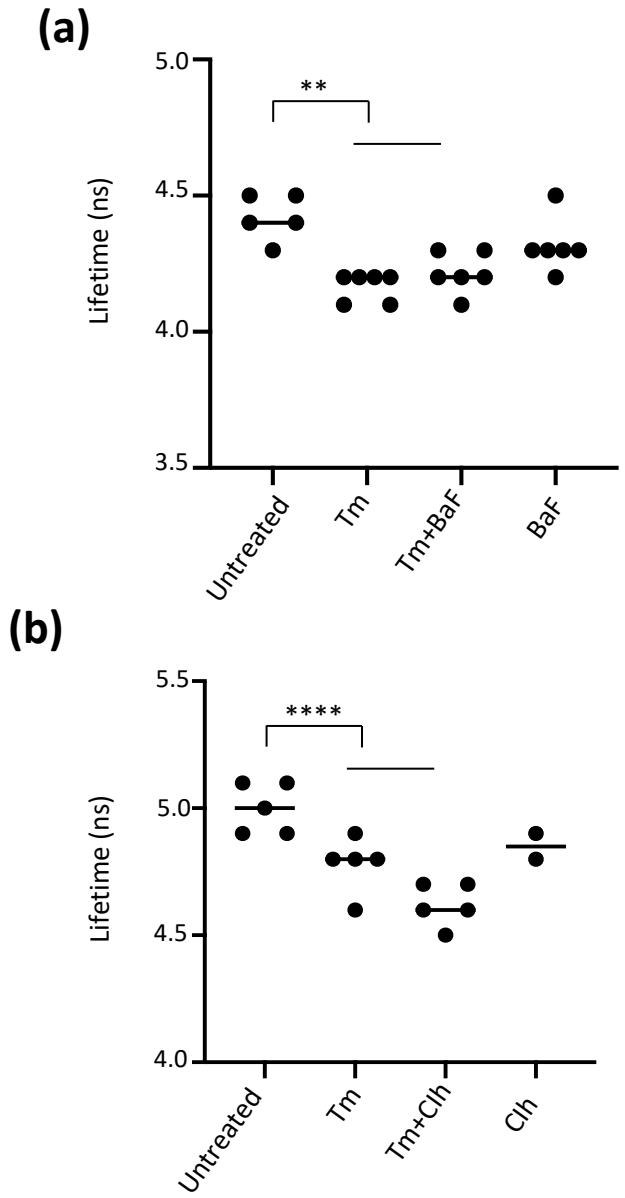
(a)
5.0
4.5
4.0
3.5
Lifetime (ns)
**
Untreated
Tm
Tm+BaF
BaF
(b)
5.5
5.0
4.5
4.0
Lifetime (ns)
****
Untreated
Tm
Tm+Clh
Clh

Fig. S7

**(a)**

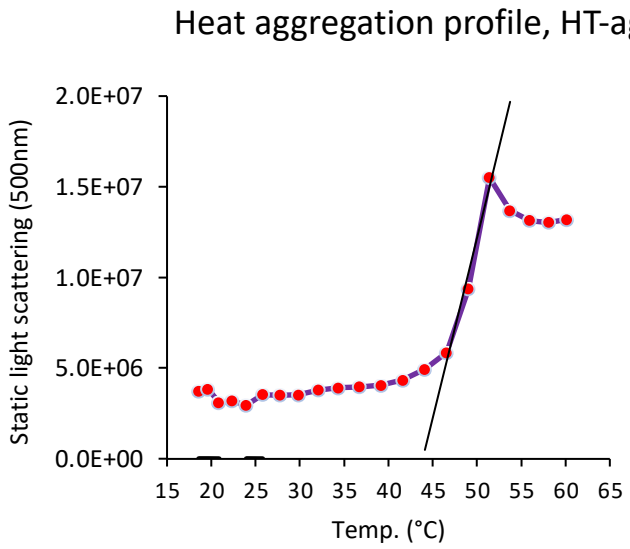
Heat aggregation profile, HT-aggr-JD
Static light scattering (500nm)
2.0E+07
1.5E+07
1.0E+07
5.0E+06
0.0E+00
15 20 25 30 35 40 45 50 55 60 65
Temp. (°C)

**(b)**

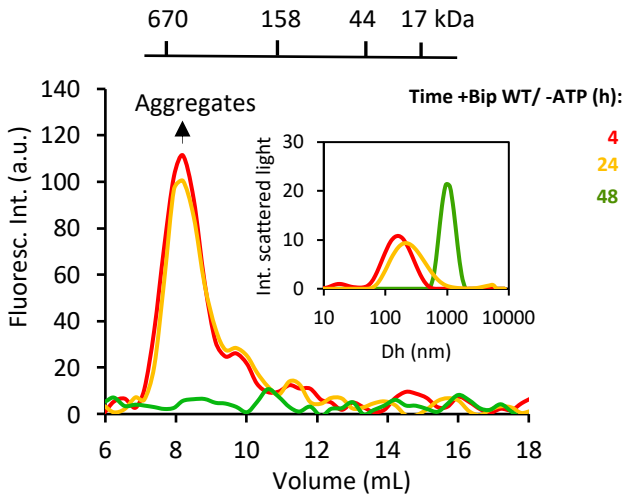
670 158 44 17 kDa
Aggregates
Time +Bip WT/ -ATP (h):
4
24
48
Fluoresc. Int. (a.u.)
140 120 100 80 60 40 20 0
6 8 10 12 14 16 18
Volume (mL)
Int. scattered light
30 20 10 0
10 100 1000 10000
Dh (nm)

## List of plasmids

| Plasmid name | Expression host | Encoded protein | Origen |
|---|---|---|---|
| SP_H6_HaloK73T_KDEL_pCMV1 | Mammalian ER | HT-K73T | This Study* |
| pFLAG_HaloK73T_cyto | Mammalian cytosol | HT-K73T | This Study* |
| SP_H6_Halo_WT_KDEL_pBABEpu | Mammalian ER | HT-WT | This Study* |
| SP_H6_Halo_K73T_KDEL_pBABEpu | Mammalian ER | HT-K73T | This Study* |
| SP_H6_Halo_L172Q_KDEL_pBABEpu | Mammalian ER | HT-L172Q | This Study* |
| SP_H6_Halo_M21K_F86L_KDEL_pBABEpu | Mammalian ER | HT-M21KF86L | This Study* |
| pLVS-VG | Mammalian | Retroviral packaging | - |
| pJK3 | Mammalian | Retroviral packaging | - |
| pCMV_TATTAT_HIV | Mammalian | Retroviral packaging | - |
| pET30_Halotag_K73T_v2 | Bacterial | HT-K73T | This study |
| pET30_Halotag_K73T_Jdomain | Bacterial | HT-K73T_Jdomain | This study |
| haBiP_27-654_pQE10 | Bacterial | BiP-WT | PMID: 22869598 |
| haBiP_27-654_V461F_pQE10 | Bacterial | BiP-V461F | PMID: 22869598 |

* ER targeted variants made based on Halotag-ER from PMID: 30224760, K73T mutation identified in PMID: 28557281.